Available online at www.sciencedirect.com
ScienceDirect
Acta Materialia 57 (2009) 2440–2453
Acta MATERIALIA
www.elsevier.com/locate/actamat

Contribution of non-octahedral slip to texture evolution of fcc polycrystals in simple shear

M. Arzaghi, B. Beausir, L.S. Tóth *

Laboratoire de Physique et Mécanique des Matériaux, Université Paul Verlain de Metz, Ile du Saulcy, 57045 Metz, France

Received 22 November 2008; received in revised form 28 January 2009; accepted 29 January 2009
Available online 9 March 2009

Abstract

The contribution of non-octahedral $\{100\}\langle 110\rangle$ slip to texture evolution under simple shear in face-centred cubic (fcc) polycrystals was studied. It was found that, by adding the $\{100\}\langle 110\rangle$ slip system family to the usual $\{111\}\langle 110\rangle$, the ideal orientations remain the same. However, the stability of the ideal orientations, the rotation field and the rate of change of the orientation density function were affected by the non-octahedral slip activity. The stress state, the slip distribution and the form of the equipotential functions were also examined along the ideal fibres. Finally, the texture evolution in pure aluminium during equal channel angular extrusion was simulated and analysed.
© 2009 Acta Materialia Inc. Published by Elsevier Ltd. All rights reserved.

Keywords: Ideal orientations; Non-octahedral slip; Textures; Simple shear; Equal channel angular extrusion

1. Introduction

Aluminium and its alloys are widely used mainly for their light weight compared with other metals. In order to improve their mechanical properties, severe plastic deformation (SPD) is often applied by different processes, e.g. equal channel angular extrusion (ECAE [1]), high pressure torsion [2], accumulated roll bonding [3] or, more recently, high pressure tube twisting [4].

SPD processes impose usually large shear deformation in the material, involving very significant texture development, which in turn affects the final mechanical properties of the material. Thus, simulations of the texture evolution during SPD are of great importance not only for a quantitative description of the forming process, but also to account for the anisotropy in the physical properties of the product.

Experiments revealed that, in addition to the usual $\{111\}\langle 110\rangle$ face-centred cubic (fcc) slip systems, non-octahedral (NOC) glide is also a possible deformation mechanism in aluminium [5]. Several NOC slip system families were identified: $\{100\}\langle 110\rangle$, $\{112\}\langle 110\rangle$ and $\{110\}\langle 110\rangle$. Among them, the most significant contribution is attributed to the $\{100\}\langle 110\rangle$ family, because the $\{100\}$ planes are the most densely packed after $\{111\}$. Bacroix and Jonas [6] examined the effect of deformation temperature on texture development in high stacking fault energy metals. For this purpose, they took into account the possibility of the activation of new slip systems or cross-slip in a rate-insensitive analysis by employing the full constraints (Taylor) model. After finding out that the introduction of NOC slip does not really improve the rolling textures observed at high temperatures, they simulated the effect of cross-slip, which led to better simulation results. It is shown in the present paper that strain rate sensitivity is a very important element in the slip process which could not be taken into account in the study of Bacroix and Jonas [6].

Increasing temperature leads to the activation of several deformation mechanisms, i.e. non-compact slip, dislocation climb, diffusion processes, recrystallization, cross-slip [7–10]. Maurice and Driver [11] studied hot rolling textures

* Corresponding author. Tel.: +33 387547238; fax: +33 387315366.
E-mail address: toth@univ-metz.fr (L.S. Tóth).

1359-6454/$36.00 © 2009 Acta Materialia Inc. Published by Elsevier Ltd. All rights reserved.
doi:10.1016/j.actamat.2009.01.041

in high-temperature plane strain compression in Al alloy crystals both experimentally and numerically, employing both the self-consistent models [12,13] and the Taylor full constraints and relaxed constraints models. They showed that, by incorporating several NOC slip system families with equal reference strengths, the simulations resulted in better hot rolling texture predictions than using only the usual $\{111\}\langle 110\rangle$ family. They studied only the high-temperature case and suggested that the adaptation of their work for hot torsion textures would be of great interest. It is important to note that, for all models, they used a relatively high strain rate sensitivity exponent for the crystallographic slip, which is in accord with the findings of the present study.

In the present work, a detailed analysis of the effect of $\{100\}\langle 110\rangle$ NOC glide on the stability of the ideal orientations and the shape of the yield potential surface is presented during simple shear of aluminium using rate-dependent slip. First, the persistence characteristics as well as the velocity field of the ideal orientations are examined. Then, the second part is devoted to an analysis of the stress state and the slip distribution around the ideal positions, together with the shape of the stress-equipotentials. It was found that the addition of NOC slip does not change the ideal orientations; only the relative intensities of the texture components changes. Finally, the texture development in ECAE is modelled to illustrate the main findings of the first two theoretical sections. Two ECAE experiments are simulated: first pass of route A, and fifth pass of route B_c. The main finding is that NOC slip improves the simulation of texture development, especially at large strains.

2. Fundamental relations

Simple shear deformation with a shear rate $\dot{\gamma} = \sqrt{3}\,\mathrm{s}^{-1}$ was imposed on fcc crystals defined by the following velocity gradient in a rectangular reference system (x_1, x_2, x_3):

$$\underline{\underline{L}} = \begin{pmatrix} 0 & \dot{\gamma} & 0 \\ 0 & 0 & 0 \\ 0 & 0 & 0 \end{pmatrix} \tag{1}$$

This shear rate corresponds to a von Mises equivalent strain-rate of $\bar{\dot{\varepsilon}} = 1.0\,\mathrm{s}^{-1}$. For polycrystals, the Taylor hypothesis was used, according to which $\underline{\underline{L}}$ is the same for all crystals. For crystallographic slip, the well-known rate-dependent constitutive law was employed [14]:

$$\tau^{\mathrm{s,f}} = \tau_0^{\mathrm{f}}\ \mathrm{sgn}\left(\dot{\gamma}^{\mathrm{s,f}}\right)\left|\frac{\dot{\gamma}^{\mathrm{s,f}}}{\dot{\gamma}_0}\right|^m = \tau_0^{\mathrm{f}}\left(\frac{\dot{\gamma}^{\mathrm{s,f}}}{\dot{\gamma}_0}\right)\left|\frac{\dot{\gamma}^{\mathrm{s,f}}}{\dot{\gamma}_0}\right|^{m-1} \tag{2}$$

Here $\tau^{\mathrm{s,f}}$ is the resolved shear stress in the slip system, indexed by 's', of the family, indexed by 'f', $\dot{\gamma}^{\mathrm{s,f}}$ is the slip rate, τ_0^{f} is the reference stress level (at which the slip rate is $\dot{\gamma}_0$), and m is the strain rate sensitivity index. The reference stress τ_0^{f} was assumed to be the same within a given slip system family but could be different from one family to the other. Hereafter, the reference stresses will be referred as τ_0^{OC} and τ_0^{NOC} for the octahedral and NOC slip system families, respectively. The ratio r between these two reference stresses is an important parameter which characterizes the relative strengths of the two slip system families:

$$r = \tau_0^{\mathrm{NOC}}/\tau_0^{\mathrm{OC}} \tag{3}$$

In the present work, an analysis of the orientation persistence of the crystals is presented under plastic strain (elastic distortions are neglected). For this purpose, it is necessary to distinguish between three types of rotations. They are: the material spin $\underline{\underline{\beta}}$, the plastic spin $\underline{\underline{\omega}}$ and the lattice spin $\underline{\underline{\Omega}}$. The material spin is the skew-symmetric part of the velocity gradient $\underline{\underline{L}}$ relative to the fixed laboratory reference system:

$$\beta_{ij} = \frac{L_{ij} - L_{ji}}{2} \tag{4}$$

The plastic spin $\underline{\underline{\omega}}$ is the skew-symmetric part of the velocity gradient corresponding to plastic slip only, with respect to the fixed reference system; it is given by [15,16]:

$$\omega_{ij} = \sum_{f=1}^{\mathrm{nf}} \sum_{s=1}^{\mathrm{nsf}} \frac{m_{ij}^{\mathrm{s,f}} - m_{ji}^{\mathrm{s,f}}}{2}\dot{\gamma}^{\mathrm{s,f}} \tag{5}$$

where $\underline{\underline{m}}$ is the Schmid orientation tensor of a slip system. Finally, the lattice spin $\underline{\underline{\Omega}}$ is the rate of rotation of the crystallographic directions with respect to the fixed reference system. (The index 'nf' denotes the total number of families, and 'nsf' is the number of slip system in family 'f'.) The following relation exists between the above-defined spin quantities [17]:

$$\underline{\underline{\Omega}} = \underline{\underline{\beta}} - \underline{\underline{\omega}} \tag{6}$$

A crystal orientation can be identified by a vector $\underline{g}$, which is defined by the three Euler angles $\underline{g} = (\varphi_1, \varphi, \varphi_2)$. Using a crystal plasticity model, the corresponding rotation velocity field $\dot{\underline{g}} = (\dot{\varphi}_1, \dot{\varphi}, \dot{\varphi}_2)$ can be calculated for any $\underline{g}$. The following relation relates the lattice spin $\underline{\underline{\Omega}}$ to the transformation matrix $\underline{\underline{T}}$, which expresses the orientation of the crystal axes with respect to the laboratory frame:

$$\dot{\underline{\underline{T}}} = \underline{\underline{\Omega T}} \tag{7}$$

$\underline{\underline{T}}$ is constructed with the help of the Euler angles. Using Eq. (7), the components of $\dot{\underline{g}}$ can be obtained [18,19]:

$$\begin{aligned} \dot{\varphi}_1 &= \Omega_{12} - \dot{\varphi}_2 \cos\varphi, \\ \dot{\varphi} &= \Omega_{32}\cos\varphi_1 - \Omega_{13}\sin\varphi_1, \\ \dot{\varphi}_2 &= (\Omega_{32}\sin\varphi_1 - \Omega_{13}\cos\varphi_1)/\sin\varphi. \end{aligned} \tag{8}$$

The $\underline{\underline{T}}$ matrix expresses the same transformation as the $\underline{g}$ vector. $\underline{\underline{T}}$ and $\underline{g}$ are, however, mathematically different quantities; this is the reason why the orientation change is calculated from Eq. (8). In this way, the updating of the Euler angles leaves $\underline{\underline{T}}$ orthogonal, even at large strains.

3. Influence of NOC slip on the lattice spin

3.1. Orientation persistence

The original technique proposed by Tóth et al. [20] for evaluating the persistence characteristics of fcc structures was based on a parameter P obtained from the lattice spin $\underline{\underline{\Omega}}$ using the following definition:

$$P(\underline{g},\underline{\dot{\varepsilon}}) = \ln\frac{\bar{\dot{\varepsilon}}}{\left\|\Omega(\underline{g},\underline{\dot{\varepsilon}})\right\|} \quad \text{with} \quad \|\underline{\underline{\Omega}}\| = \sqrt{\Omega_{12}^2+\Omega_{31}^2+\Omega_{23}^2} \tag{9}$$

where $\bar{\dot{\varepsilon}}$ is the von Mises equivalent strain rate. One difficulty with this parameter is that it can become infinity when $\underline{\underline{\Omega}} = 0$. Although it does not happen for simple shear – when the slip is rate sensitive [20,21] – it can happen for other deformation modes, such as rolling [22]. Thus, in order to have persistence parameter that can be calculated for any deformation mode and for any orientation, the following new definition is proposed here:

$$P\left(\underline{g},\underline{\dot{\varepsilon}}\right) = 1 - \left(\left|\Omega\left(\underline{g},\underline{\dot{\varepsilon}}\right)\right| \Big/ \Omega_{\max}\right)^{1/3} \tag{10}$$

Here, $\Omega_{\max}$ is the maximum value of $\|\underline{\underline{\Omega}}\|$ in the whole Euler space, and $\underline{\dot{\varepsilon}}$ is the strain rate tensor. In this way, the P parameter varies between 0 and 1. The exponent 1/3 was chosen so that, when P is plotted in orientation space, its map resembles an orientation density function (ODF) of a well-developed deformation texture.

In previous stability studies and experimental work [20,23–43], two ideal fibres, i.e. where the persistence of grain orientations is high, were identified. They are the A

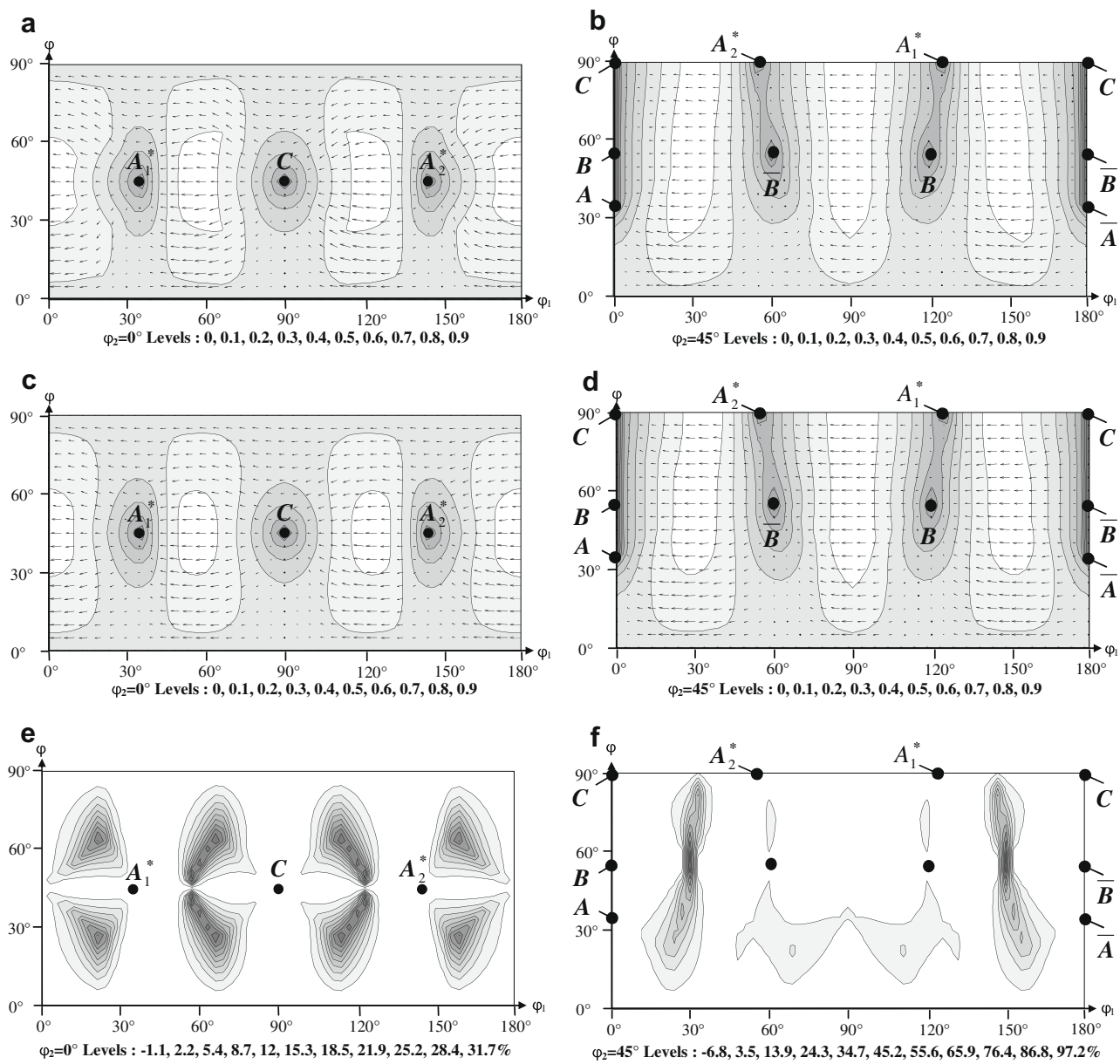

Fig. 1. (a–d) Orientation persistence maps in Euler space ($m = 0.05$) for OC only and OC+NOC slips, respectively. (e and f) Maps of the change in stability parameter by adding the OC+NOC slip systems.

fibre $\{1\,1\,1\}\langle uvw\rangle$ and the B fibre $\{hkl\}\langle 1\,1\,0\rangle$, where $\{hkl\}$ identifies the shear plane and $\langle 1\,1\,0\rangle$ is the shear direction. They can be obtained by rotating a grain initially oriented in the $(1\,1\,\bar{1})[1\,\bar{1}\,0]$ position around the shear plane normal (A fibre) or around the shear direction (B fibre).

The persistence parameter as defined in Eq. (10) was calculated in the whole Euler space for different combinations of the two slip system families. The value of P depends on the strain rate sensitivity index m; the value of $m = 0.05$ was used in the present work. This choice of m was based on modelling of deformation texture development. Indeed, by decreasing m further, the texture development remains very similar [35]. Fig. 1 shows maps of the persistence parameter in two sections of the whole Euler space; $\varphi_2 = 0°$ and $\varphi_2 = 45°$. Only these sections were selected for the following two reasons: (1) these two sections contain all ideal components of simple shear textures; (2) in this way, the space required for plotting the whole map is reduced, which permits more detail to be shown. Fig. 1a and b displays P for the classical case when NOC slip is not activated, while Fig. 1c and d shows P when the resistances of both slip system families are equal: $\tau_0^{OC} = \tau_0^{NOC}$, that is when $r = 1$. The three-dimensional velocity field $\underline{\dot{g}} = (\dot{\varphi}_1, \dot{\varphi}, \dot{\varphi}_2)$ is also projected on these two sections and is examined in the following section.

A comparison of the persistence maps presented in Fig. 1 shows that there is no difference in the position of the ideal orientations, and there are no new stable components when NOC slip is added to the octahedral slip system family. The ideal positions remain the same as previously reported in experimental work [23–31,33,34,36,37,39] as well as in modelling [20,30,32,35,38–43]. There are, nevertheless, differences in the value of the persistence parameter. Fig. 1e and f shows the differences in percentages in the same two sections defined as follows:

$$d = 100 \times \left(P^{OC+NOC} - P^{OC}\right)/P^{OC+NOC} \tag{11}$$

Here, P^{OC} means the persistence only for octahedral slip, and P^{OC+NOC} is for the case when both octahedral and NOC slips are allowed. Thus, d can reach ~30% in certain zones of the $\varphi_2 = 0°$ section and nearly 100% in the $\varphi_2 = 45°$ section. However, the zones where d is significantly different from zero are located far from the ideal positions, thus NOC slip affects the lattice rotation of those orientations which are not near the ideal positions. (There are some small differences also along the A fibre, which will be discussed separately below.) Another observation is that, with NOC slip, the stability parameter is globally larger than when the classical octahedral slip is considered alone. It means that the lattice spin decreases with NOC slip activity (at same time, the plastic spin increases; see Eq. (6)). Thus, the activity of NOC slip decreases the lattice rotation when the grains are oriented far from the ideal orientations; consequently, grain orientations will be slower to reach the ideal positions with increasing plastic strain. So, it is expected that the speed of the texture evolution reduces when NOC slip occurs.

Fig. 2 represents the stability parameter P along the A and B fibres calculated numerically for $m = 0.05$ and for the OC and OC+NOC glide cases, respectively. Along the A fibre, P attains its minimum and maximum values at the $A/\bar{A}$ and A_1^*/A_2^* orientations, respectively (A_2^* is not shown in the A fibre, but its P value is the same as for A_1^*). When NOC slip is added with equal strength, the maximum and minimum are reversed, and P decreases all along the A and B fibres. Along the B fibre, the maximum value of P is located at the A and $\bar{A}$ orientations, and the minimum is at the C for octahedral slip. While P is decreasing in general all along the B fibre when NOC slip is activated, P remains unchanged for the C orientation. As a consequence, the maximum value of P, located at A and $\bar{A}$ for octahedral slip can be found between A and B (the same between $\bar{A}$ and $\bar{B}$) when NOC slip is added. Note that, along the two fibres, the stability parameter does not reach

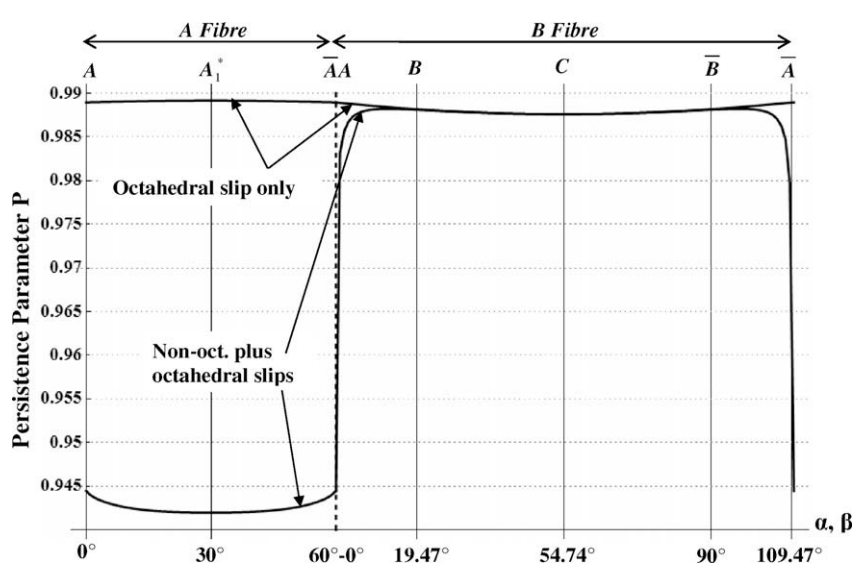

Fig. 2. Dependence of the stability parameter P on position along the A and B fibres. For the A fibre, the curve is repeated every 60°.

the limiting value of 1.0, which would correspond to zero lattice spin. This is an effect of the rate sensitivity of slip and has already been discussed in [20] for octahedral slip. It means that, under rate-sensitive conditions, there is no permanent ideal orientation along the ideal A and B fibres.

Fig. 2 shows that NOC slip affects the orientation persistence mainly along the ideal A fibre. Nevertheless, the value of P changes by only a few per cent (~5% maximum). These relatively small changes in P are not expected to affect the texture evolution drastically. However, it will be shown in the following that texture evolution is significantly affected by the activity of the NOC slip both in experiments and in simulations. In order to understand the effects of NOC slip on the texture development, it is necessary to examine the rotation field and the rate of change of the ODF in the whole orientation space.

3.2. Rotation field

The crystallographic texture of a polycrystal is best described by the ODF denoted by $f(\underline{g})$. In order to understand the changes that can take place during large plastic deformation, both the rotation field $\dot{\underline{g}} = (\dot{\varphi}_1, \dot{\varphi}, \dot{\varphi}_2)$ and the rate of change of $f(\underline{g})$ must be examined. These two elements are the main ingredients of the continuity equation of texture development [18,19,44,45], which can be obtained in the following way. The crystal deformation mechanism considered here (i.e. crystallographic slip) preserves volume; consequently, the polycrystal volume fraction contained in an elementary volume of orientation space $\delta\underline{g} = \sin(\varphi)\delta\varphi_1\delta\varphi\delta\varphi_2$ remains constant during macroscopic shearing:

$$\frac{d\left(f\delta\underline{g}\right)}{d\gamma} = \delta\underline{g}\frac{df}{d\gamma} + f\frac{d\left(\delta\underline{g}\right)}{d\gamma} = f\delta\underline{g}\left[\frac{d\ln f}{d\gamma} + \frac{d\ln\left(\delta\underline{g}\right)}{d\gamma}\right] = 0 \tag{12}$$

Deriving $\delta\underline{g}$ with respect to γ, one obtains:

$$\begin{aligned}\frac{d\left(\delta\underline{g}\right)}{d\gamma} &= \frac{1}{\dot{\gamma}}\delta\underline{g}\left[\dot{\varphi}\cot\varphi + \frac{\partial\dot{\varphi}_1}{\partial\varphi_1} + \frac{\partial\dot{\varphi}}{\partial\varphi} + \frac{\partial\dot{\varphi}_2}{\partial\varphi_2}\right] \\ &= \frac{1}{\dot{\gamma}}\delta\underline{g}\left[\dot{\varphi}\cot\varphi + \mathrm{div}\left(\dot{\underline{g}}\right)\right]\end{aligned} \tag{13}$$

Using these two equations, the continuity equation can be written (in the Lagrangian formulation):

$$\dot{\gamma}\frac{d\ln f}{d\gamma} + \dot{\varphi}\cot\varphi + \mathrm{div}\left(\dot{\underline{g}}\right) = 0 \tag{14}$$

Similarly, in the Eulerian formulation:

$$\dot{\gamma}\frac{d\ln f}{d\gamma} + \dot{\varphi}\cot\varphi + \mathrm{div}\left(\dot{\underline{g}}\right) + \dot{\underline{g}}\cdot\mathrm{grad}(\ln f) = 0 \tag{15}$$

Note that, for $\dot{\underline{g}} = 0$ (the case of ideal orientations), Eqs. (14) and (15) are equivalent. The rate of change of the ODF intensity at a given orientation is characterized by the term $\dot{\gamma}\cdot(d\ln f/d\gamma)$, which can be deduced from Eq. (15). For relatively weak textures, $\dot{\underline{g}}\mathrm{grad}(\ln f)$ can be neglected because both $\dot{\underline{g}}$ and $\mathrm{grad}(\ln f)$ are small near the ideal orientations.

From the viewpoint of texture formation, a texture component at orientation $\underline{g}$ can be considered stable during deformation as long as

$$\dot{\underline{g}} = (\dot{\varphi}_1, \dot{\varphi}, \dot{\varphi}_2) = 0 \quad \text{and} \quad \dot{\gamma}\frac{d\ln f}{d\gamma} > 0 \tag{16}$$

In previous works [46–48], only the $\mathrm{div}(\underline{g})$ quantity was used to characterize the divergent/convergent nature of the orientation flow. However, the $\dot{\gamma}(d\ln f/d\gamma)$ quantity represents better the changes that take place in the ODF during plastic strain and thus, in the present work, this quantity, which can be readily obtained from Eq. (15) by neglecting the $\dot{\underline{g}}\mathrm{grad}(\ln f)$ term, will be examined. In order to shorten the notation, this term will be denoted by $\mathrm{div}^{(\varphi)}$ because, basically, it is the $\mathrm{div}(\dot{\underline{g}})$ quantity including the $\dot{\varphi}\cot\varphi$ correction term, which accounts for the distortion of the Euler space that exists along the φ coordinate.

Fig. 3 shows both $\dot{\underline{g}} = (\dot{\varphi}_1, \dot{\varphi}, \dot{\varphi}_2)$ and the $\mathrm{div}^{(\varphi)}$ quantities in two sections of Euler space; $\varphi_2 = 0°$ and $\varphi_2 = 45°$ for the OC and OC+NOC cases. $\mathrm{div}^{(\varphi)}$ is calculated from Eq. (15) at grids points of Euler space separated by 2°, while $\dot{g}$ is represented on a grid of 5° using Eq. (7). Dark regions correspond to $\mathrm{div}^{(\varphi)} < 0$ while, in the light regions, $\mathrm{div}^{(\varphi)} > 0$. Black bold lines are placed at the boundaries of these regions ($\mathrm{div}^{(\varphi)} = 0$). The arrows are the projections of the $\underline{g}$ vectors. The strain rate sensitivity index m is 0.05 and $r = 1$.

In these diagrams, there is overall orientation accumulation (convergence) where $\mathrm{div}^{(\varphi)} < 0$ (dark areas), and divergence where $\mathrm{div}^{(\varphi)} > 0$ (light areas). The shapes of these regions are globally the same for OC and OC+NOC glides. Note that all ideal orientations are situated at the boundary lines: that is, at positions where $\mathrm{div}^{(\varphi)} = 0$.

This is one of the main characteristics of shear textures which was also observed in previous work for fcc [46,49], bcc [47] and hcp [48] crystal structures. As shown in Fig. 3, the contribution of NOC glide decreases the intensity of $\mathrm{div}^{(\varphi)}$ (that is the rate of change of the ODF) by ~12% in the $\varphi_2 = 0°$ section whereas, in the $\varphi_2 = 45°$ section, no significant change happens.

The rotation field in the vicinity of the ideal orientations A, $\overline{A}$, B, $\overline{B}$, A_1^*, A_2^* and C are shown in $\varphi_2 = cst$ sections of the Euler space in Fig. 4. The $\varphi_2 = cst$ section was selected because the velocity field is globally more affected by NOC glide in the $\varphi_2 = cst$ sections than in the φ or φ_1 sections. Red and black arrows are the projections of the $\underline{g}$ vectors for OC and OC+NOC glides, respectively. As shown in Fig. 4, the main lattice rotation takes place in the direction of the rigid body spin imposed by the test. The axis of this rotation is axis 3; this is why orientations drift mainly along the $-\varphi_1$ direction in Euler space. This trend does not change when NOC glide is added. Next, the rotation fields around the ideal orientations are examined one by one:

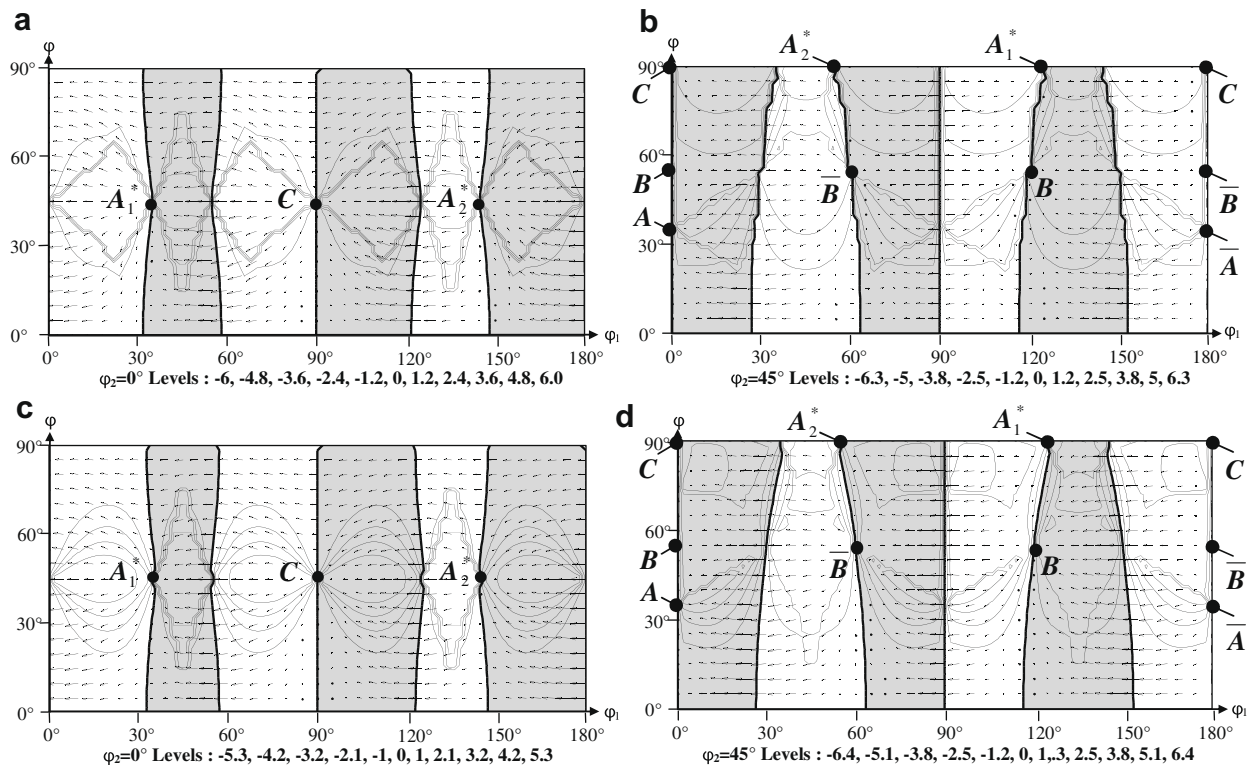

Fig. 3. Iso-value map of the rate of change of the ODF ($m = 0.05$). The light and dark regions correspond to accumulation and migration of the grains, respectively.

3.2.1. A_1^* region

The velocity field in the accumulative zone (right side) of A_1^* is not affected by NOC glide, while on the left side it is strongly modified. The grains quit the vicinity of the A_1^* orientation in the φ direction faster, which indicates a faster decrease in the intensity of the A_1^* orientation once NOC glide is present.

3.2.2. A_2^* region

The direction of grain rotation remains the same in the divergent region (left side) with NOC glide, while the velocity is increased. As for the accumulative zone, on the right side, the rotation field becomes more parallel to the rigid body rotation when NOC is active. These changes in the rotation field mean that the catchment area of the A_2^* texture component is decreased when NOC glide is present and, consequently, one can expect that the intensity of this component will be reduced with respect to the case when only OC glide is operational.

3.2.3. C region

When NOC is active, the direction of the velocity field remains the same on the bottom side of the C orientation, but the grains rotate more slowly. On the top side, the rotation field becomes more parallel to the rigid body rotation without significant change in the velocity values. These characteristics should lead to slightly lower intensity of the C component when NOC slip is activated. In any case, the C component has the largest catchment area of grain orientations, and is thus expected to be the main texture component when the texture is initially random.

3.2.4. A and $\overline{A}$ regions

The rotation fields for these two orientations are the same; this is why both of them are indicated in Fig. 4. With respect to the other ideal orientations, these regions are less affected by the presence of NOC slip.

3.2.5. B and $\overline{B}$ regions

The same observation can be made as for the A and $\overline{A}$ above.

In general, when NOC glide is active, the grains move towards all ideal orientations with reduced speed, and they also leave the accumulation zones more slowly. Thus, under the same amount of shear, a smaller ODF intensity is expected around the ideal orientations when NOC glide is considered. This feature is in accordance with observations in Section 3.1, where the stability maps were examined (Fig. 1e and f).

4. Stress and slip analysis

In this section, the effect of NOC slip on the slip distribution and on the stress state is analysed along the A and B fibres. The general flow potential function in stress space is also examined.

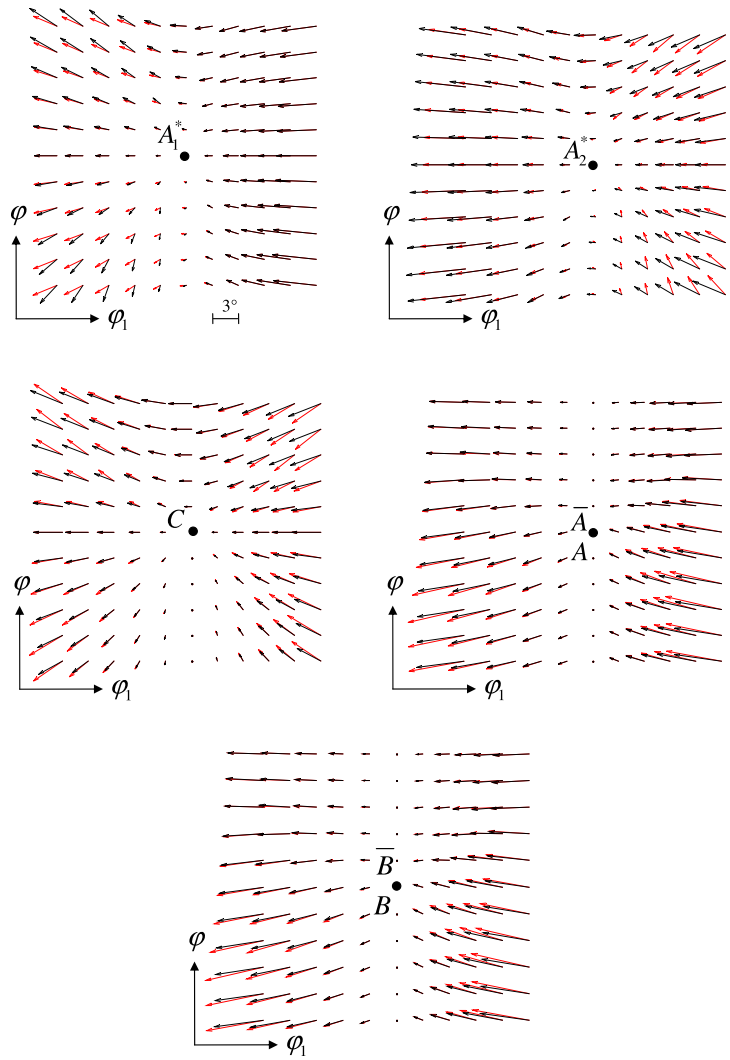

Fig. 4. The rotation field around the ideal orientations for two sections of the Euler space (in red OC, in black OC+NOC). The frames are 30° × 30° with 3° spacing. (For interpretation of the references to color in this figure legend, the reader is referred to the web version of this paper.)

4.1. Stress and slip activity along the fibres

The true stress $\underline{\underline{\sigma}}$ is related to the deviator stress $\underline{\underline{S}}$ by the hydrostatic stress p as follows:

$$\sigma_{ij} = S_{ij} + p\delta_{ij} \tag{17}$$

where δ_{ij} is the Kronecker delta. In a simple shear test, there is no traction on the lateral surfaces normal to axis 3, which imposes the boundary condition $\sigma_{33} = 0$. Thus, the hydrostatic stress can be obtained from Eq. (17) as $p = -S_{33}$. Using this relation in Eq. (17), one obtains

$$\sigma_{22} = S_{22} - S_{33} \tag{18}$$

for the axial stress acting normal to the shear plane.

Along the B fibre, the stress state is relatively simple, as there are only two components of the stress tensor that are non-zero: the S_{12} and S_{13} shear components. (Actually, with all normal components being zero, the B fibre does not contribute to axial stresses in simple shear.) Fig. 5 shows these non-zero shear stress components that were calculated

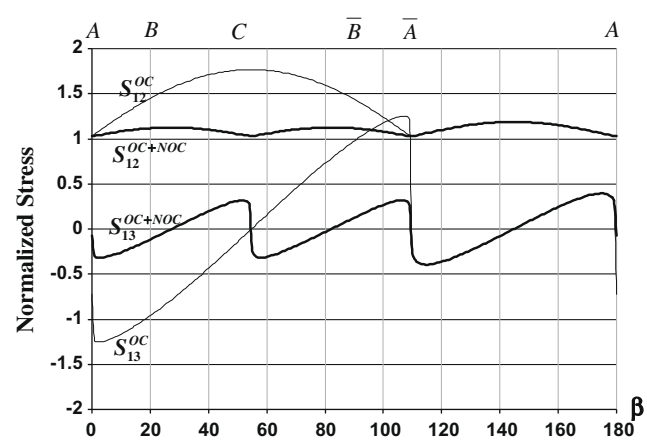

Fig. 5. The non-zero stress components associated with the B fibre pertaining for a rate sensitivity $m = 0.05$. Continuous narrow lines and bold lines are for the OC and OC+NOC cases, respectively.

Table 1
Values of the microscopic shear on ideal positions for fcc structures under simple shear considering OC slip only and OC+NOC slips[a].

	Slip systems	A_1^*: $\varphi_1 = 35.26°$, $\varphi = 45°$, $\varphi_2 = 0°$		A_2^*: $\varphi_1 = 144.74°$, $\varphi = 45°$, $\varphi_2 = 0°$		$\overline{A}$: $\varphi_1 = 180°$, $\varphi = 35.26°$, $\varphi_2 = 45°$		A: $\varphi_1 = 0°$, $\varphi = 35.26°$, $\varphi_2 = 45°$		C: $\varphi_1 = 90°$, $\varphi = 45°$, $\varphi_2 = 0°$		$\overline{B}$: $\varphi_1 = 180°$, $\varphi = 54.74°$, $\varphi_2 = 45°$		B: $\varphi_1 = 0°$, $\varphi = 54.74°$, $\varphi_2 = 45°$	
		OC	OC+NOC	OC	OC+NOC	OC	OC+NOC	OC	OC+NOC	OC	OC+NOC	OC	OC+NOC	OC	OC+NOC
Octahedral slip system family	$(1\,1\,\bar{1})\langle 0\,1\,1\rangle$	–	–	–	–	–	–	–	–	–	–	–	–	–	–
	$(1\,1\,\bar{1})\langle 1\,0\,1\rangle$	0.9997	0.99976	–	−0.00007	–	–	–	–	–	–	–	–	–	–
	$(1\,1\,\bar{1})\langle 1\,\bar{1}\,0\rangle$	0.9997	0.99976	–	−0.00007	1.73181	1.73160	1.73181	1.73160	–	–	1.83711	1.22461	1.83711	1.22461
	$(1\,\bar{1}\,\bar{1})\langle 0\,1\,\bar{1}\rangle$	–	–	0.00024	–	–	–	–	–	−1.5	−0.00003	–	–	–	–
	$(1\,\bar{1}\,\bar{1})\langle 1\,0\,1\rangle$	–	–	–	−0.00012	–	–	–	–	–	–	–	–	–	–
	$(1\,\bar{1}\,\bar{1})\langle 1\,1\,0\rangle$	–	0.00008	–	–	0.00014	0.00025	0.00014	0.00025	–	–	–	–	–	–
	$(1\,\bar{1}\,1)\langle 0\,1\,1\rangle$	–	–	–	–	–	–	–	–	–	–	–	–	–	–
	$(1\,\bar{1}\,1)\langle 1\,0\,\bar{1}\rangle$	−0.00003	0.00016	−0.99995	−0.99975	–	–	–	–	–	–	–	–	–	–
	$(1\,\bar{1}\,1)\langle 1\,1\,0\rangle$	−0.00003	0.00016	−0.99995	−0.99975	0.00014	0.00025	0.00014	0.00025	–	–	–	–	–	–
	$(1\,1\,1)\langle 0\,1\,\bar{1}\rangle$	–	–	0.00024	–	–	–	–	–	−1.5	−0.00003	–	–	–	–
	$(1\,1\,1)\langle 1\,0\,\bar{1}\rangle$	–	0.00008	–	–	–	–	–	–	–	–	–	–	–	–
	$(1\,1\,1)\langle 1\,\bar{1}\,0\rangle$	–	–	–	−0.00012	–	–	–	–	–	–	−0.6125	–	−0.6125	–
Non-octahedral	$(1\,0\,0)\langle 0\,1\,1\rangle$		–		–		–		–		–		–		–
	$(1\,0\,0)\langle 0\,1\,\bar{1}\rangle$		0.00005		0.00022		–		–		−1.73201		–		–
	$(0\,1\,0)\langle 1\,0\,1\rangle$		0.0001		–		–		–		–		–		–
	$(0\,1\,0)\langle 1\,0\,\bar{1}\rangle$		–		0.00014		–		–		–		–		–
	$(0\,0\,1)\langle 1\,1\,0\rangle$		–		−0.00014		–		–		–		–		–
	$(0\,0\,1)\langle 1\,\bar{1}\,0\rangle$		−0.0001		–		−0.00012		−0.00012		–		−0.70726		−0.70726

[a] The exact values for the angles equal to 35.26°, 54.74° and 144.74° are $\arccos(\sqrt{2/3})$, $\arcsin(\sqrt{2/3})$, $(90° + \arcsin(\sqrt{2/3}))$, respectively.

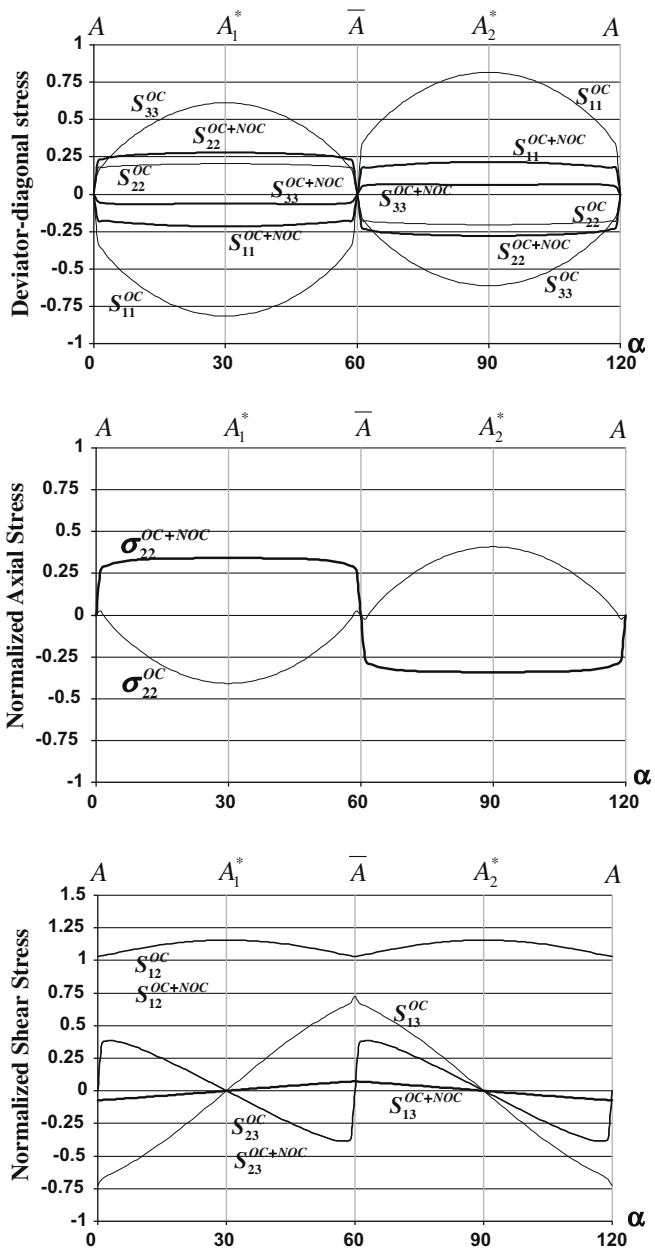

Fig. 6. (a) The deviator-diagonal, (b) the shear plane normal and (c) the shear components of the stress tensor normalized by τ_0^{OC} associated with the A fibre for $m = 0.05$. Continuous narrow lines and bold lines are for the OC and OC+NOC cases, respectively.

numerically in the sample reference axes as a function of the position along the fibre: the β angle. Both cases, with or without NOC slip, are plotted on the same figure and for $m = 0.05$. Note that the B fibre is restricted to the interval of $0° \leqslant \beta \leqslant 109.47°$. Fig. 5 shows that the S_{13} and S_{12} components are strongly affected by the activity of the NOC slip along the stable part of the B fibre. In contrast, between $\overline{A}$ and A, along the unstable part of the B fibre ($109.47° \leqslant \beta \leqslant 180°$), NOC glide does not modify the stress state.

Concerning the individual ideal orientations, Table 1 presents the active slip systems for OC and OC+NOC glides. It is clear from this table that the slip system selection is strongly affected in the B, $\overline{B}$ and C ideal positions by adding NOC glide. Indeed, the C ideal orientation passes from double slip to single slip by switching to a NOC slip system. (The very small slip rates in other slip systems are due to the non-zero $m = 0.05$ strain rate sensitivity value taken in the calculation; in the strain rate-insensitive limit, they are expected to vanish.) In the B and $\overline{B}$ orientations, there is double slip, and one of the OC slip systems is replaced by a NOC slip system when NOC is added. In A and $\overline{A}$, there is no change in the slip activity and, consequently, the stress state remains the same. Actually, $S_{13} = 0$ in the exact ideal position for A and $\overline{A}$. These changes in the slip systems are in coherence with the differences in the stress states that are displayed in Fig. 5. One can say that, globally, NOC glide decreases the variations in the stress state along the ideal B fibre.

Along the A fibre, the deviator-diagonal, the axial and the shear stress components (expressed in the sample reference system) are plotted in Fig. 6a–c, respectively. These diagrams show that, generally, all the components of the stress tensor are non-zero and that they can be of order S_{12}. As a consequence, the A fibre contributes to the axial stresses that appear during simple shear. Note that the normal stress components shown in Fig. 6a are all deviator stresses, because elastic deformation is not considered in this work, only plastic slip.

The axial stress along the A fibre obtained by Eq. (18) is plotted in Fig. 6b, which shows that it is compressive between $\overline{A}$ and A ($60° < \alpha < 120°$) and tensile between the A and $\overline{A}$ ($0° < \alpha < 60°$) portions of the fibre when only OC slip is active. This situation, however, is inverted when NOC slip is added to OC slip. There is no change in the shear stress components S_{12} and S_{23}; however, S_{13} is strongly influenced by the presence of NOC slip; it tends to zero all along the A fibre. As shown in Table 1, in the A_1^* and A_2^* ideal orientations, the same OC slip systems remain active even if the NOC slip systems are available. This is quite interesting, because the axial stress state changes radically (see above). It means that the there is only a displacement of the stress state on the hyper-planes corresponding to the active slip systems on the yield surface when NOC slip systems are added.

4.2. Stress potential functions

As shown by the results presented above, the presence of NOC slip can strongly influence the slip system selection as well as the stress state of the ideal orientations in simple shear. In order to understand better the changes in the stress states, it is useful to examine the changes in the yield surface that are induced by the presence of NOC slip systems. It is important to emphasize, however, that, as there is no yield stress threshold for strain-rate-sensitive slip corresponding to Eq. (2), a yield surface in its classical sense does not exist. However, the possible stress states can still be visualized with the help of a stress potential function. The shapes of the yield potentials give direct information about the plastic anisotropy of the

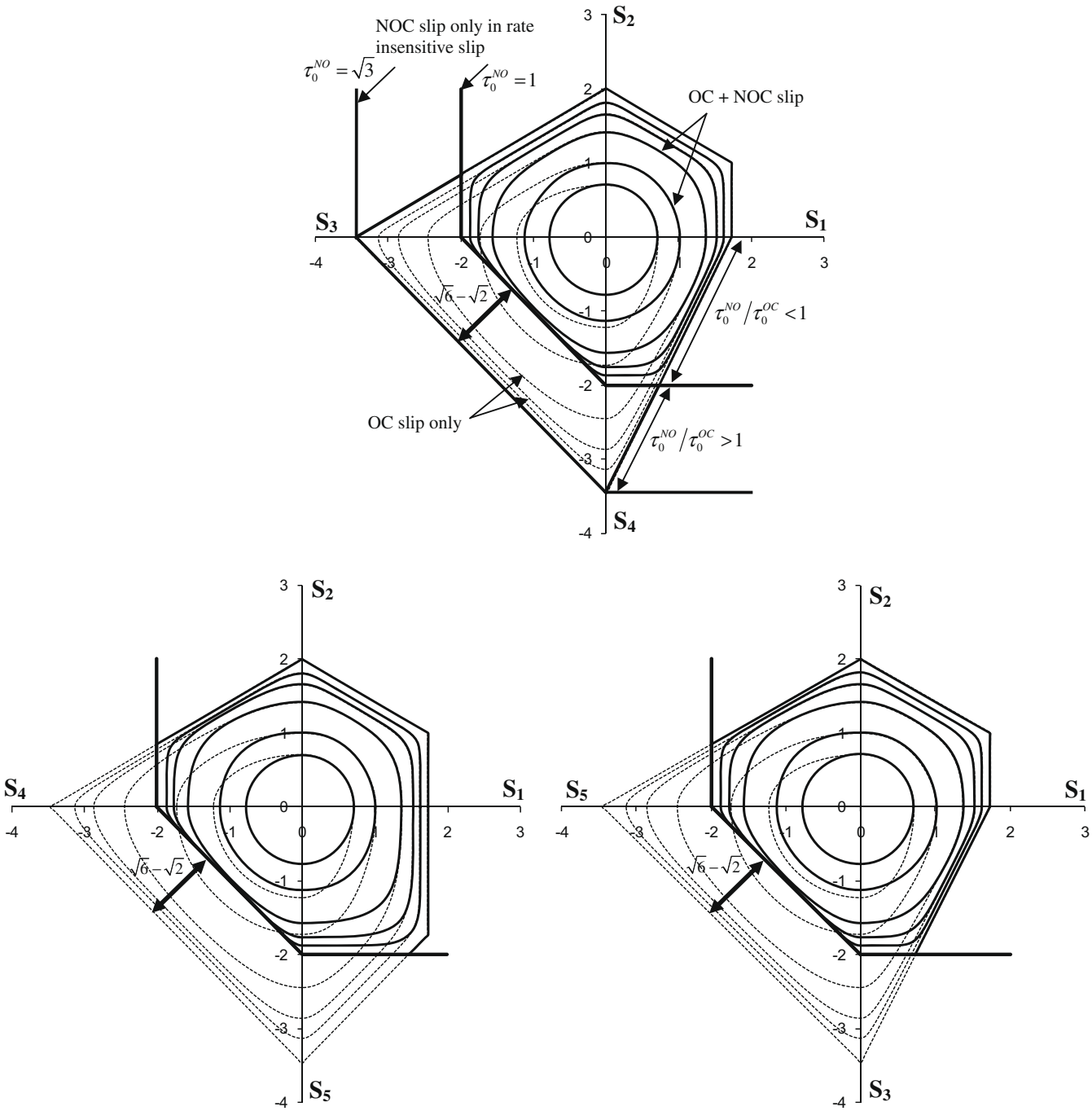

Fig. 7. Stress equi-potentials $f(S)$ in fcc crystal structures for all the possible sections in Lequeu stress space, for different values of strain rate sensitivity ($m = 1, 0.5, 0.2, 0.1, 0.05, 0$). (The smallest surface corresponds to $m = 1$.) Dotted lines represent the octahedral slip only, the largest bold line the NOC slip only in rate-insensitive glide, and the bold lines the case where $\tau_0^{\mathrm{NOC}} = \tau_0^{\mathrm{OC}} = 1.0$ MPa.

crystal. Such analysis was carried out for fcc single crystals by Tóth et al. [20] and for hcp crystals by Beausir et al. [48]. In the following, a similar analysis is proposed to examine the effect of NOC slip on the yield potentials for fcc crystal structures.

Considering the fact that only the deviator part of the stress affects the resolved shear stress, $\underline{\underline{\sigma}}$ can be replaced by $\underline{\underline{S}}$. Hence, it is possible to reduce the dimension of the stress space. For this purpose, five-component vector quantities are introduced for the deviator stress $\underline{\underline{S}}$, the strain rate $\underline{\dot{\varepsilon}}$ and the slip system orientation factor $\underline{\underline{M}}$ with the help of Lequeu's notation [50]:

$$\underline{S} = \left(\frac{(S_{22} - S_{11})}{\sqrt{2}}, \frac{\sqrt{3}}{\sqrt{2}} S_{33}, \sqrt{2} S_{23}, \sqrt{2} S_{31}, \sqrt{2} S_{12} \right), \tag{19}$$

$$\underline{\dot{\varepsilon}} = \left(\frac{(\dot{\varepsilon}_{22} - \dot{\varepsilon}_{11})}{\sqrt{2}}, \frac{\sqrt{3}}{\sqrt{2}} \dot{\varepsilon}_{33}, \sqrt{2} \dot{\varepsilon}_{23}, \sqrt{2} \dot{\varepsilon}_{31}, \sqrt{2} \dot{\varepsilon}_{12} \right), \tag{20}$$

$$\underline{M}^{s,f} = \left(\frac{\left(m_{22}^{s,f} - m_{11}^{s,f}\right)}{\sqrt{2}}, \frac{\sqrt{3}}{\sqrt{2}} m_{33}^{s,f}, \frac{\left(m_{23}^{s,f} + m_{32}^{s,f}\right)}{\sqrt{2}}, \frac{\left(m_{31}^{s,f} + m_{13}^{s,f}\right)}{\sqrt{2}}, \times \frac{\left(m_{12}^{s,f} + m_{21}^{s,f}\right)}{\sqrt{2}} \right) \tag{21}$$

An equipotential is defined so that the plastic power $\dot{W}$ is constant along its surface; i.e.

$$\dot{W} = S_i \dot{\varepsilon}_i = \sum_{f=1}^{nf} \sum_{s=1}^{ns} \tau^{s,f} \dot{\gamma}^{s,f} = C \tag{22}$$

With the help of Eq. (2) and knowing that the resolved shear stress is related to the deviator stress tensor $\underline{\underline{S}}$ by $\tau^{s,f} = m_{ij}^{s,f} S_{ij}$, $\dot{W}$ becomes:

$$\dot{W} = \sum_{f=1}^{nf} \frac{\dot{\gamma}_0}{\left(\tau_0^f\right)^{1/m}} \sum_{s=1}^{ns} \left| M_i^{s,f} S_i \right|^{\frac{1}{m}+1} = C \tag{23}$$

A property of the stress potential function $f(\underline{S})$ is that the plastic strain-rate (in vector form) is normal to it:

$$\dot{\varepsilon}_i = \frac{\partial f(\underline{S})}{\partial S_i} \tag{24}$$

Under this condition, $f(\underline{S})$ can be expressed as:

$$F(\underline{S}) = \frac{m}{m+1} \sum_{f=1}^{nf} \frac{\dot{\gamma}_0}{\left(\tau_0^f\right)^{1/m}} \sum_{s=1}^{ns} \left| M_i^{s,f} S_i \right|^{\frac{1}{m}+1} = C \tag{25}$$

In the present work, the equipotentials were calculated in the crystal reference system for all cases; for OC slip alone, for NOC slip and finally for OC+NOC. A series of strain rate sensitivity index values were considered: $m = 1, 0.5, 0.2, 0.1, 0.05$ and 0. The constant C in the expression of $f(\underline{S})$ (Eq. (25)) was chosen as: $C = \tau_0^{OC} \dot{\gamma}_0 m/(m+1)$. Here, $\tau_0^{OC} \dot{\gamma}_0$ is a plastic power that corresponds to the plastic power for single slip within one octahedral slip system, where the resolved shear stress is equal to the reference strength τ_0^{OC}, and the slip rate is $\dot{\gamma}_0 = 1.0\ s^{-1}$. All obtained stress components are expressed in units of τ_0^{OC}.

Fig. 7 shows the stress equipotentials for all possible sections of the five-dimensional deviator stress space in a special representation concerning the stress axes. Namely, because the stress potentials display mirror symmetries as well as centro-symmetry, it is possible to use two stress components on the same axis line (separated by the origin) which permits four sections to be represented on the same graph. The dotted lines, the bold solid lines and the solid lines correspond to the classical octahedral slip only, the NOC slip only and to OC+NOC slips with $r = 1$, respectively. The stress potentials for the limiting case of $m = 0$ were plotted using the classical Schmid yield criterion.

Fig. 7 shows that the shapes of the equipotential surfaces become more and more rounded as the m value is increased and, as expected, sharp vertices appear in the limiting case of rate-independent behaviour ($m = 0$). Adding the NOC slip family does not change the centro-symmetry of the potential surfaces. However, when only NOC slip is considered, the stress potential is not closed. Indeed, the NOC slip family contains only three independent slip systems, and thus cannot accommodate arbitrary deformations. When both OC and NOC are considered, there is a limit value of r above which NOC slip becomes completely inactive, its value is indicated in Fig. 7: $r > \sqrt{3}$. In contrast, such a limit value does not exist to eliminate octahedral slip. The influence of NOC slip on the yield surface was examined by Bacroix and Jonas [6] for the rate-insensitive case, and similar conclusions were made.

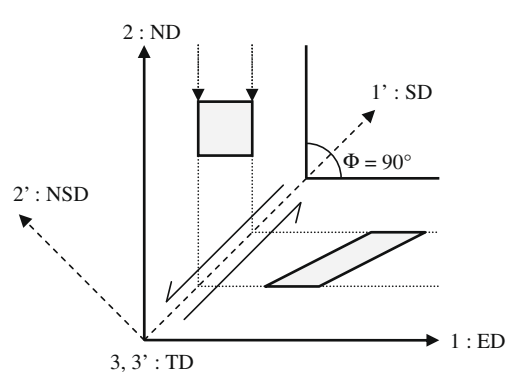

Fig. 8. ECAE schema.

5. Application to ECAE

The results of the analysis presented above concerning the effect of NOC slip in shear provide a detailed insight into the plastic behaviour of fcc crystals. This makes a good basis for understanding the textures that develop during large strain shear. For this purpose, the texture evolution in pure aluminium during ECAE is studied in the present section. The ECAE process consists of extruding a lubricated sample through two channels of equal and identical cross sections. The deformation mode is near simple shear in the intersection plane of the two channels that form the die (see Fig. 8). Although deviations exist from the so-called simple shear model (see the flow line model of Tóth et al. [51] and the FAN model of Beyerlein and Tomé [52]), it remains a good approximation in many practical cases. In the present study, the simple shear model was employed to simulate the texture development during ECAE. This approach has recently been further justified in a study using the flow lines in ECAE of Al [53].

As the deformation mode is considered to be simple shear in ECAE, the ideal orientations are the same as in simple shear, except that the reference system is rotated by +45° around the TD axis (3-axis) for a 90° die, as illustrated in Fig. 8. Consequently, the ideal positions move by +45° in the φ_1 direction of Euler space when the texture is examined in the non-rotated (1, 2, 3) reference system (see Fig. 8). The ideal positions for simple shear of fcc crystals for OC slip remain unchanged when NOC slip is added, as shown in the previous sections of this work.

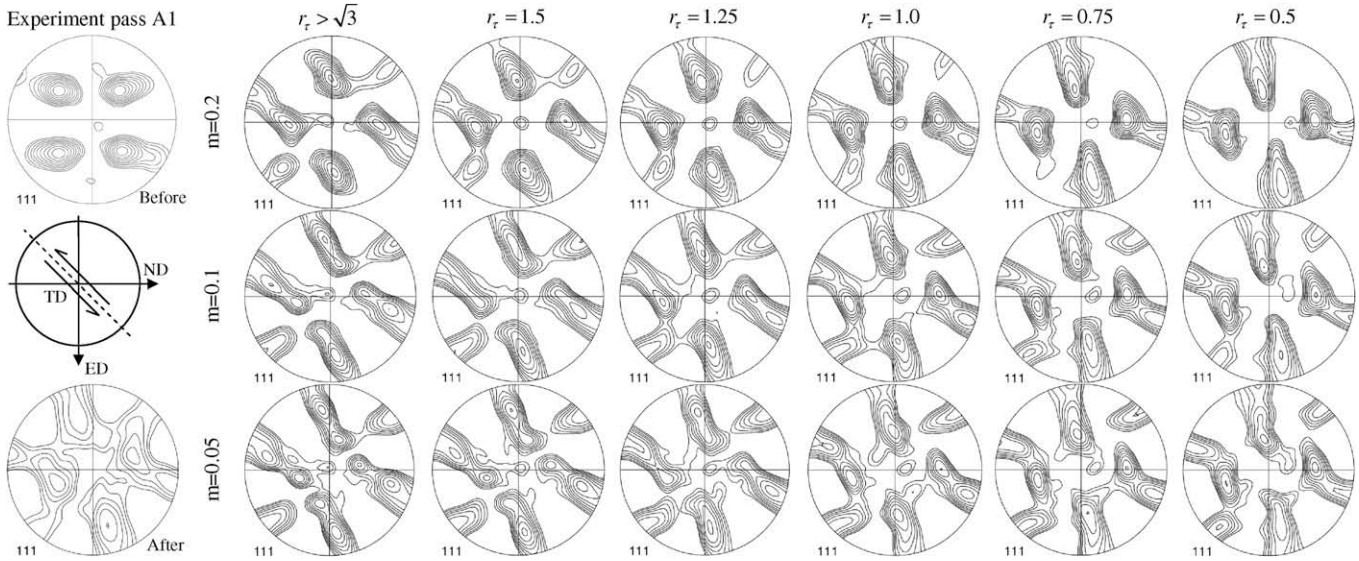

Fig. 9. (1 1 1) pole figures of experimental and simulated texture of the first pass in route A. Levels: 0.8, 1.0, 1.3, 1.6, 2.0, 2.5, 3.2, 4.0, 5.0, 6.4.

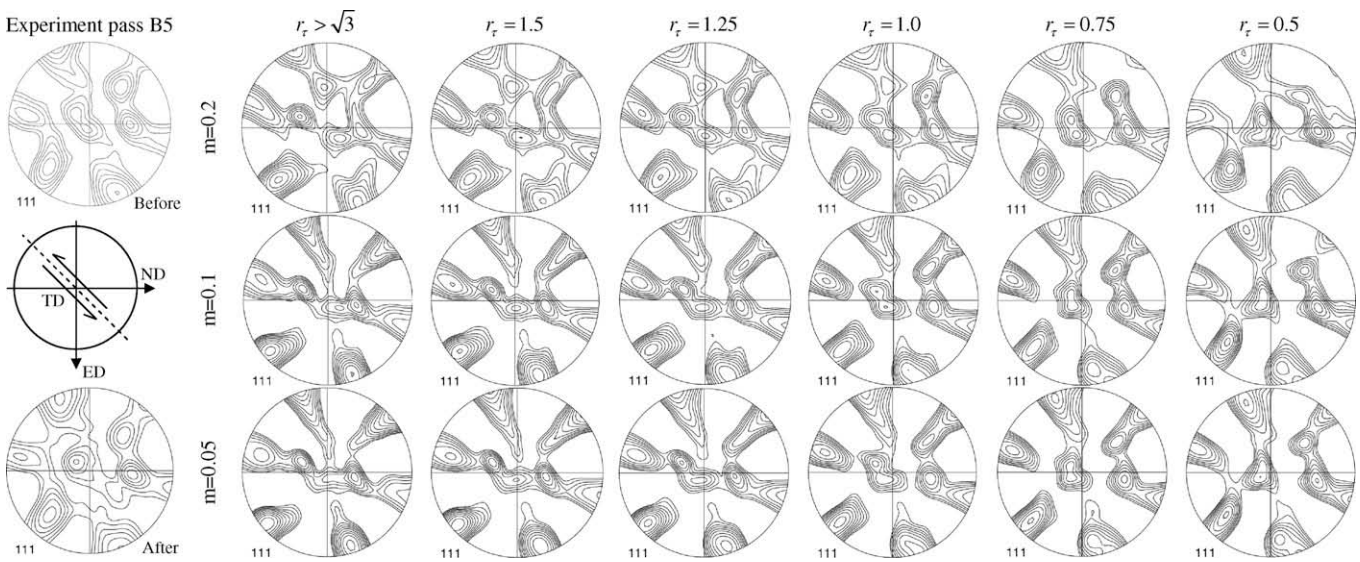

Fig. 10. (1 1 1) pole figures of experimental and simulated texture of the fifth pass in route B_c. Levels: 0.8, 1.0, 1.3, 1.6, 2.0, 2.5, 3.2, 4.0, 5.0, 6.4.

Pure aluminium was subjected to ECAE for the usual routes A, B_c and C up to five passes (see Ref. [54] for more experimental details). The experimental textures were measured by X-ray diffraction on the longitudinal middle plane of the deformed sample with normal direction. In the present work, only the texture evolution during the first pass (named A1) and the fifth pass of route B_c (named B5) are simulated (more simulation results can be found in Ref. [54]). For this purpose, the experimental input textures presented in Figs. 8 and 9 were used in the simulations: for the first pass, the texture of the as-received material; for the B5 texture, the texture after the fourth pass. The viscoplastic self-consistent model was employed for the simulations, and different values of the strain-rate sensitivity index $(m = 0.2, 0.1, 0.05)$ and $(r = \sqrt{3}, 1.5, 1.0, 0.75, 0.5)$ were employed. In the absence of available hardening data at the slip system level, the r values were kept constant in a single pass of ECAE. Figs. 9 and 10 show the experimental texture as well as several simulated textures in (1 1 1) pole figure forms for passes A1 and B5, respectively. The simulated textures are quite sensitive to both parameters, and it is quite difficult to select the parameter combination that corresponds best to the experimental texture.

In order to quantify the differences of the simulation results in comparison with the experiments, the texture index of experimental and simulated ODF was calculated in the same way as in Refs. [55–57]. The texture index was introduced by Bunge [58] as follows:

$$T = \int_{\text{Euler space}} \left[f\left(\underline{g}\right) \right]^2 d\underline{g} \tag{26}$$

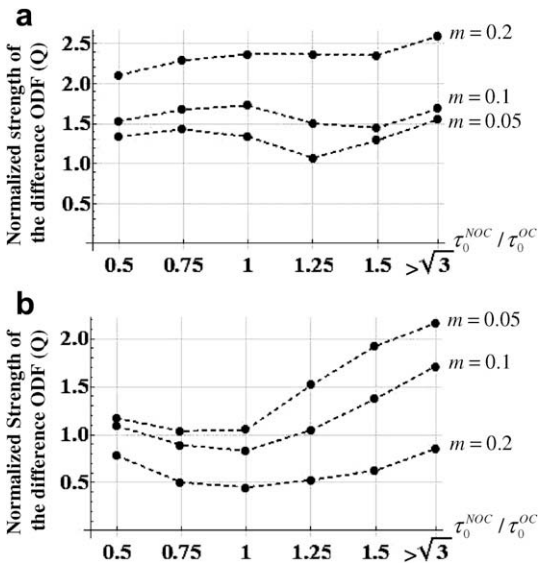

Fig. 11. The normalized texture index of the different ODF between simulations and experience for (a) the first pass route A and (b) the fifth pass route B_c.

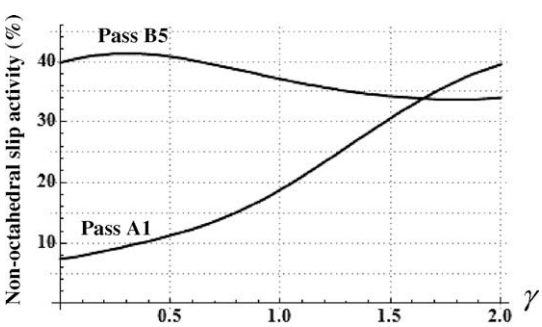

Fig. 12. Non-octahedral slip activity during the first pass route A and the fifth pass route B_c from simulation results.

The value of T increases as texture sharpens. When the difference between the simulated $f_{\text{sim}}(\underline{g})$ and experimental ODF $f_{\text{exp}}(\underline{g})$ is used in place of $f(\underline{g})$ in Eq. (26), T describes the strength of the *deviation* between the two textures. After normalizing by the texture index of the experimental texture, a parameter Q representing the 'texture-simulation quality' can be obtained:

$$Q = \frac{\int_{\text{Euler space}} \left[f_{\text{exp}}\left(\underline{g}\right) - f_{\text{sim}}\left(\underline{g}\right) \right]^2 d\underline{g}}{\int_{\text{Euler space}} \left[f_{\text{exp}}\left(\underline{g}\right) \right]^2 d\underline{g}} \tag{27}$$

The Q parameter was calculated for all the simulations and is presented in Fig. 11a and b for the A1 and B5 passes, respectively. The good simulation result corresponds to a small Q value. In this way, the optimum r value can be identified. For the first pass, the best agreement is obtained for $r = 1.25$ and for a strain-rate sensitivity index $m = 0.05$. As shown in Fig. 11a, the smaller the m, the better the simulation is for the A1 pass. However, at a large ECAE pass number, for pass B5, the best parameters are different: $r = 1$ and $m = 0.2$. Thus, for this pass, the role of the strain-rate sensitivity index m on the quality of the simulation is reversed; the larger the m, the better is the simulation. Fig. 12 presents the relative activity of non-octahedral slip during the first pass route A and the fifth pass route B from simulation results. While the activity of NOC glide remains more or less constant at ~35% during the fifth pass route B, a large increase of the activity occurs during the first pass route A, from ~10% at the beginning up to 40% at the end of the pass.

The use of a relatively large value for the strain rate sensitivity index m (=0.2) may seem unreasonable for the behaviour of aluminium at room temperature and needs discussion. Note that, in crystal plasticity, there are two distinct effects of the strain rate sensitivity that must be considered simultaneously. First, the stress equipotentials become more and more rounded when m is increased [20,48]. As a consequence, the number of active slip systems increases, and that affects the lattice spin, i.e. the texture evolution. This effect is called the 'shape effect' of the yield surface on the texture evolution and remains valid also when NOC slip occurs. The second effect is related to the amplitude of the stress state, which also depends on the strain rate sensitivity index m (see the constitutive equation, Eq. (2)). It was shown in [59] that the second effect is negligible on the texture evolution; only the form-effect is relevant.

6. Summary and conclusions

This work examined how NOC slip affects the stress state and the persistence characteristics around the ideal orientations of fcc polycrystals as well as the texture development in a simple shear test. The results obtained lead to the following general conclusions.

1. The addition of NOC slip family to the OC slip does not change the ideal orientation positions in the Euler space.
2. Grain orientations that are far from the ideal positions reach the ideal positions more slowly when NOC slip is present. Consequently, not only the speed of the texture evolution decreases, but also the intensity of the ODF is smaller around the ideal orientations under the same amount of shear when NOC slip is active.
3. When NOC slip is added, the stress state changes along both the A and B fibres, but this variation is much less pronounced on the B fibre. The axial stress is inverted by adding NOC slip, and the slip system selection is greatly affected in the B, $\overline{B}$ and C orientations.
4. The yield potential surfaces display a limit value ($\sqrt{3}$) beyond which NOC slip becomes completely inactive.
5. The use of NOC slip in the simulation of texture development in room temperature ECAE of pure Al improves the textures significantly.

References

[1] Valiev RZ, Langdon TG. Prog Mater Sci 2006;51:881.
[2] Languillaume J, Chmelik F, Kapelski G, Bordeaux F, Nazarov AA, Cavova G, Esling C, et al. Acta Metall Mater 1993;41:2953.
[3] Saito Y, Utsunomiya H, Tsuji N, Sakai T. Acta Mater 1999;47:579.
[4] Tóth LS, Arzaghi M, Fundenberger J-J, Beausir B, Bouaziz O, Arruffat-Massion R. Scripta Mater 2009;60:175.
[5] Mecif A, Bacroix B, Franciosi P. Acta Mater 1997;45:371.
[6] Bacroix B, Jonas JJ. Texture Microstruct 1988;8:267.
[7] Argon AS, Haasen P. Acta Mater 1993;41:3289.
[8] Anongba P, Bonneville J, Martin JL. Acta Mater 1993;41:2907.
[9] Carrard M, Martin JL. Philos Mag A 1988;58:491.
[10] Howe S, Liebmann B, Lüe K. Acta Metall 1961;9:625.
[11] Maurice CI, Driver JH. Acta Mater 1997;45:4639.
[12] Lebensohn RA, Tomé CN. Acta Metall 1993;41:2611.
[13] Molinari A, Tóth LS. Acta Metall 1994;42:2453.
[14] Hutchinson JW. Proc Roy Soc Lond 1976:101.
[15] Havner KS. Proc Roy Soc Lond 1981;378:329.
[16] Havner KS. Philos Trans Roy Soc 1984;311:469.
[17] Havner KS. Acta Mech 1972:183.
[18] Clement A, Coulomb P. Scripta Metall 1979;13:899.
[19] Gilormini P, Tóth LS, Jonas JJ. Proc Roy Soc Lond 1990;430:489.
[20] Tóth LS, Gilormini P, Jonas JJ. Acta Metall 1988;36:3077.
[21] Beausir B, Suwas S, Tóth LS, Neale KW, Fundenberger J-J. Acta Mater 2008;56:200.
[22] Tóth LS, Jonas JJ, Daniel D, Ray RK. Metall Trans 1990;21A:2985.
[23] Backofen WA. Trans AIME 1950;188:1454.
[24] Backofen WA, Hundy BB. Trans AIME 1953;197:1953.
[25] Williams RO. Trans Metall Soc AIME 1962;224:129.
[26] Regenet PJ, Stüwe PH. Z Metallk 1963;54:273.
[27] Stüwe PH, Turck H. Z Metallk 1964;55:699.
[28] Rose W, Stüwe PH. Z Metallk 1968;59:396.
[29] Witzel W. Z Metallk 1973;64:813.
[30] Gil Sevillano J, Van Houtte P, Aernoudt E. Z Metallk 1975;66:367.
[31] Gil Sevillano J, Van Houtte P, Aernoudt E. Scripta Metall 1977;11:581.
[32] Van Houtte P, Aernoudt E. Mater Sci Eng 1976;23:11.
[33] Van Houtte P, Aernoudt E, Sekine K. In: Nagashima S, editor. Proceedings of the ICOTOM6, Tokyo, Japan. Japan: Iron Steel Institute; 1981. p. 337.
[34] Sekine K, Van Houtte P, Gil Sevillano J, Aernoudt E. In: Nagashima S, editor. Proceedings of the ICOTOM6, Tokyo, Japan. Japan: Iron Steel Institute; 1981. p. 395.
[35] Canova GR, Kocks UF, Jonas JJ. Acta Metall 1984;32:211.
[36] Montheillet F, Cohen M, Jonas JJ. Acta Metall 1984;32:2077.
[37] Montheillet F, Gilormini P, Jonas JJ. Acta Metall 1985;33:705.
[38] Bacroix B. Ph.D. Thesis, McGill University, Montreal; 1986.
[39] Hughes DA, Wenk HR. In: Kallend JS, Gottstein G, editors. Proceedings of the ICOTOM8. Santa Fe, N.M.: Metallurgical Society; 1987. p. 455.
[40] Lowe TC, Asaro RJ. In: Kallend JS, Gottstein G, editors. Proceedings of the ICOTOM8. Santa Fe, N.M.: Metallurgical Society; 1987. p. 325.
[41] Molinari A, Canova GR, Ahzi S. Acta Metall 1987;35:2983.
[42] Harren S, Lowe TC, Asaro RJ, Needleman A. Philos Trans Roy Soc 1989;328:443.
[43] Tóth LS, Jonas JJ. In: Kallend JS, Gottstein G, editors. Proceedings of the ICOTOM8. Santa Fe, N.M.: Metallurgical Society; 1987. p. 337.
[44] Clement A. Mater Sci Eng 1982;55:203.
[45] Arminjon M. J Méca Théor Appl 1987;6:511–23.
[46] Tóth LS, Neale KW, Jonas JJ. Acta Metall 1989;37:2197.
[47] Baczynski J, Jonas JJ. Acta Mater 1996;44:4273.
[48] Beausir B, Tóth LS, Neale KW. Acta Mater 2007;55:2695.
[49] Neale KW, Tóth LS, Jonas JJ. Int J Plasticity 1990;6:45.
[50] Lequeu P, Gilormini P, Montheillet F, Bacroix B, Jonas JJ. Acta Metall 1987;35:439.
[51] Tóth LS, Arruffat-Massion R, Germain L, Baik SC, Suwas S. Acta Mater 2004;52:1885.
[52] Beyerlein IJ, Tomé CN. Mater Sci Eng 2004;380:171.
[53] Hasani A, Tóth LS. Scripta Mater, in press.
[54] Suwas S, Arruffat-Massion R, Tóth LS, Fundenberger J-J, Beausir B., submitted for publication.
[55] Li S, Beyerlin IJ, Necker CT, Alexander DJ, Bourke M. Acta Mater 2004;52:4859.
[56] Li S, Beyerlin IJ, Alexander DJ, Vogel SC. Acta Mater 2005;53:2111.
[57] Suwas S, Aruffat-Massion R, Tóth LS, Fundenberger J-J, Eberhardt A, Skrotzki W. Metall Mater Trans 2006;37A:739.
[58] Bunge HJ. Texture analysis in materials science, mathematical methods. London: Butterworth; 1982.
[59] Tóth LS, Qods F, Fundenberger J-F. Z Metallk 2005;96:1038.